Int J Adv Manuf Technol (2016) 86:1375–1384
DOI 10.1007/s00170-015-8280-y

ORIGINAL ARTICLE

A characterization of microstructure and mechanical properties of A6N01S-T5 aluminum alloy hybrid fiber laser-MIG welded joint

Qiuying Wang[1] · Hui Chen[1] · Zongtao Zhu[1] · Peixian Qiu[2] · Yunlong Cui[2]

Received: 10 August 2015 / Accepted: 17 December 2015 / Published online: 9 January 2016
© Springer-Verlag London 2016

Abstract A6N01S-T5 aluminum alloy is used widely on components of high-speed train body, such as the sidewall and underframe. Welded joints are often the positions where fracture and failure occur. In this paper, fiber laser-metal inert gas (MIG) welding was used as a new welding method to weld A6N01S-T5 alloy and compared with the traditional MIG welding joints. Optical microscopy, scanning and transmission electron microscopy, hardness tester, and electronic universal testing were used for the microstructure observation and mechanical property examination. Softening effect in the heat affected zone (HAZ) and weld fusion zone is observed. The precipitations and dissolution of β′ phases are proved to be the reason of softening. The tensile strength of the fiber laser-MIG welded joint was approximately 83 % of base metal, which is 33 MPa higher than that of the MIG welded joint. The fracture position of the joints is in accordance with the lowest hardness position.

Keywords Aluminum alloy · Hybrid welding · Microstructure · Mechanical properties

1 Introduction

Al-Mg-Si (6xxx series) alloys have good extrusion property, welding ability, and corrosion resistance [1]. High-speed train is developing very rapidly in recent years where A6N01S-T5 Al alloy finds wide applications including high-speed train body and a number of components. In the manufacturing of these Al alloy components, conventional fusion welding methods (especially metal inert gas (MIG) welding) are commonly used [2, 3]. However, softening of Al alloy is unavoidable when the conventional fusion welding methods are used. With the loss of mechanical properties, large residual stresses and deformation are the common problems in welding of Al alloys. In order to obtain better welded joints, different welding methods are used. Hybrid laser-arc welding is one of them.

Hybrid welding can provide enhanced productivity and capabilities in excess of what can be achieved by either laser or arc welding alone [4, 5]. In recent years, studies on the hybrid laser-arc welding are a hot topic in the welding of Al alloys. There are investigations on the stability and parameter optimization in hybrid laser-arc welding of Al alloys [6–10]. Studies on the microstructure and mechanical properties of hybrid laser-arc welded joints have also been reported [11–13]. Al-Mg-Si alloy system gains their strength via precipitation strengthening, which is sensitive to thermal process [2]. Softening behavior of Al-Mg-Si alloy joints by hybrid laser-arc welding has been studied [14]. However, the studies are almost all on the sheets thinner than 6 mm. Studies on the hybrid laser-arc welding of thick plates are rarely reported [15].

Mechanical properties of A6N01S-T5 alloy are different when the thickness changes from less than 6 to ~12 mm according to JIS H 4100:2006. A6N01S-T5 extruded sheets of 2–4 mm thick are used as sidewalls, floors, and roofs of high-speed train body [2, 3]. However, A6N01S-T5 extruded sheets with thicknesses more than 6 mm are usually used in the underframes. Studies on hybrid laser-arc welding of Al alloys (especially Al-Mg-Si alloys) are far from completion.

✉ Hui Chen
xnrpt@swjtu.edu.cn

[1] School of Materials Science and Engineering, Southwest Jiaotong University, Chengdu, Sichuan 610031, China

[2] CRRC Qingdao Sifang Co., Ltd., Qingdao, Shandong 266000, China

Table 1 Composition of the A6N01 alloy and ER5356 wire (wt%)

Element	Si	Fe	Cu	Mn	Mg	Cr	Zn	Ti	Al
A6N01	0.501	0.107	0.023	0.205	0.491	0.166	0.005	0.027	Bal.
ER5356[a]	≤0.25	≤0.40	≤0.10	0.05–0.20	4.5–5.5	0.05–0.20	≤0.10	0.06–0.20	Bal.

[a] Other elements: each ≤0.05, total ≤0.15

This work uses fiber laser-MIG welding to weld 8-mm-thick A6N01S-T5 alloy. Microstructure, hardness, and tensile property of the joints were studied. Analysis on the microstructure and precipitated phases of the joints was carried out. The relationship between microstructure and hardness was discussed, and the tensile strength was compared with that of the MIG welded joints.

2 Experimental procedure

In this study, 8-mm-thick A6N01S alloy in T5 state was butt welded. The welding wire used was a commercial ER5356 wire of 1.2 mm in diameter. Their chemical compositions are given in Table 1, and the mechanical properties of A6N01S-T5 are listed in Table 2. Welding was carried out along the rolling direction of the samples with the size of 300 × 120 mm, after pre-weld cleaning.

The welding experiments were carried out by a combination of an IPG YLS-4000 fiber laser (4-kW maximum output power) and KEMPPI KempArc Pulse 450 welding machine, which were controlled by an ABB IRB-2600 industrial robot. The wavelength and diameter of the fiber laser were 1.06 and 200 μm, separately. Schematic diagram of hybrid welding setup is shown in Fig. 1. The processing parameters of hybrid welding are presented in Table 3. Schematic diagram of Y-shape groove used in laser-MIG hybrid welding is shown in Fig. 2a.

In order to optimize the welding parameters, a large number of hybrid welding experiments were carried out. According to weld appearance and the results of digital radiography, the suitable welding process parameters of laser-MIG hybrid welding are presented in Table 4. In order to compare the mechanical properties of laser-MIG hybrid welded and MIG welded joints, single-pulse MIG welding of A6N01S-T5 was also carried out with V-shape groove (Fig. 2b), and the parameters are shown in Table 4.

Table 2 Mechanical properties of A6N01S-T5

Tensile strength (MPa)	Percentage of elongation $A_{80\ mm}$ (%)	Hardness (HV3)
292	17.12	91

In order to investigate the thermal cycles of the hybrid welded joint, holes were bored at 5, 10, 15, and 20 mm away from the weld center. These holes are 9 mm deep and 5 mm in diameter. K-type thermocouples (NiCr-NiSi, diameter 0.8 mm) were welded to the bottom of the holes by spot welding.

The metallographic samples were cross-sectioned perpendicular to the welding direction, then polished, and etched in Keller etchant. In order to observe the grain distribution of heat affected zone (HAZ) and base metal, 43 % HCl + 6 % HNO_3 + 1 % HF etching solution was used to the polished surface of the joint. Optical microscopy (OM) was used to observe the microstructures and grain distributions; SEM-energy-dispersive spectrometry (EDS) (HITACHI SU8010) and TEM (JEM-2010) were used to investigate precipitations.

Vicker hardness profiles were obtained by HVS-30 hardness tester in samples that were used in microstructure examinations. The load was 3000 g and lasted for 15 s. The tensile tests were conducted at the loading speed of 5 mm/min on a CM3505 electronic universal testing machine according to ISO 4136:2012. Dog-bone-shape specimens are used as shown in Fig. 3. The weld bead had been grinded away in order to ensure a constant cross section. The fracture surfaces of tensile samples were also observed by SEM.

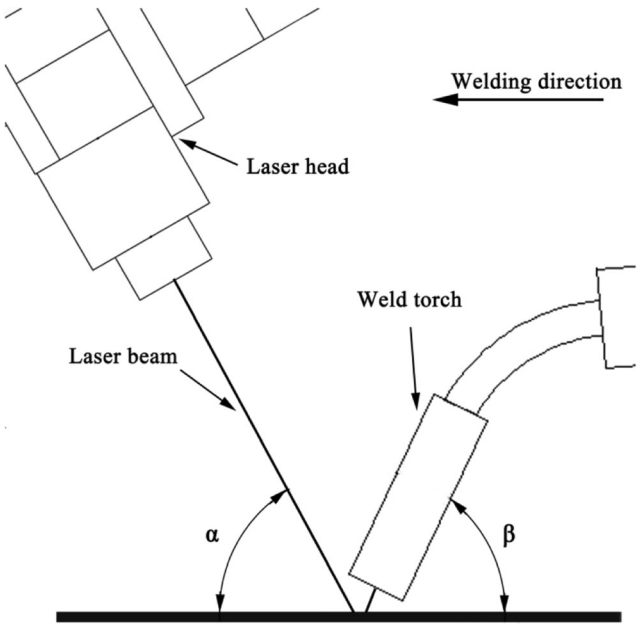

Fig. 1 Schematic diagram of hybrid welding setup

Table 3 Fixed process parameters

Parameter	Values
Laser mode	Continuous
α—the angle of laser beam to the workpiece	70°
Laser focus position	5 mm below the upper surface
Distance laser-arc	3–5 mm
β—the angle of MIG torch to the workpiece	68°
Weld stick out length	20 mm
Shielding gas	99.999 % pure argon
Shielding gas flow rate	25 L/min

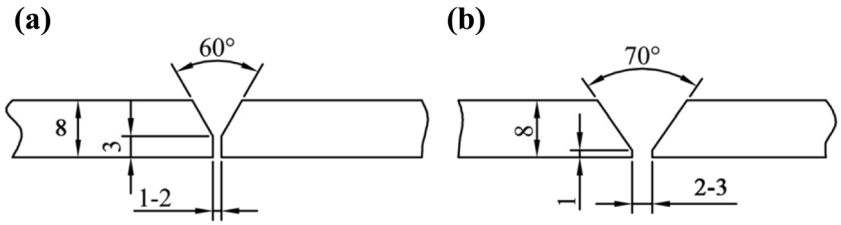

Fig. 2 Schematic diagrams of the welding groove: **a** laser-MIG welding and **b** MIG welding (unit: mm)

3 Results and discussion

3.1 Hardness distribution

The hardness distribution in the different zones of A6N01S-T5 hybrid laser-MIG welded joint is shown in Fig. 4. The distance of the test line from the top is 4 mm. The softest point of laser-MIG welded joint is 54 HV, which is at the weld fusion zone. The width of HAZ is about 20 mm. The hardness in the HAZ is lower than the base metal (91 HV) with the difference of 35 HV. The low hardness observed in the HAZ is due to the partial dissolution, over-aging, and uncontrolled particle reprecipitation during weld thermal cycle [16]. In this study, HAZ of hybrid joint can be divided into two regions: the quenched zone and over-aging zone. The region close to the partially melted zone (PMZ) is the quenched zone [2]. The region close to the base metal is over-aging zone. Positions of the weld fusion zone, quenched zone, over-aging zone, and base metal are determined according to the microstructure analysis and hardness distribution. Figure 4a shows that the softening in the over-aging zone is more severe than in the quenched zone.

The weld fusion zone of hybrid laser-MIG welded joint can be divided into arc zone and laser zone [17, 18]. Figure 4b shows the hardness of arc zone and laser zone. The two test lines are 2 and 6 mm away from the top of the sample. The average hardness of the laser zone and arc zone is 52 and 56 HV, respectively. The hardness of laser zone is slightly lower than arc zone.

3.2 Macrostructure and microstructure

Image of cross section of hybrid laser-MIG welded joint is shown in Fig. 5a. Full-penetration weld can be seen. Microstructures and grain distributions of the welded joint are shown in Figs. 5b–i and 6. The welded joint consists of weld fusion zone, PMZ, HAZ, and base metal.

Table 4 Welding process parameters

Parameters		P_{laser} (kW)	v (m/min)	I_{MIG} (A)	U_{MIG} (V)	$E_{single\ pass}$ (kJ/cm)	E_{total} (kJ/cm)
Laser-MIG		3.2	0.54	231	26.3	10.3	10.3
MIG	1	–	0.42	189	23.8	6.4	11.9
	2	–	0.42	177	21.8	5.5	

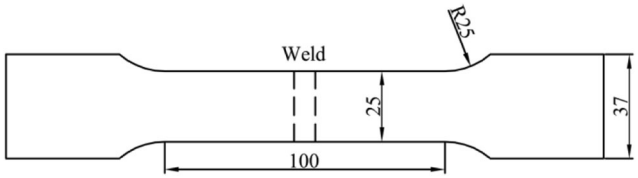

Fig. 3 Dimension of tensile specimens (unit: mm)

It can be seen from Fig. 5b–d that the dendrites are dominant in the weld fusion zone. Molten pool crystalline morphology mainly depends on the solute concentration C_0, crystallization rate R, and temperature gradient in liquid phase G. It is known that G/R determines the solidification mode and microstructure. G increases with the distance from weld center, and R decreases with the distance from weld center. Therefore, some equiaxed dendrites formed in the weld center, and columnar crystal can be observed adjacent to PMZ.

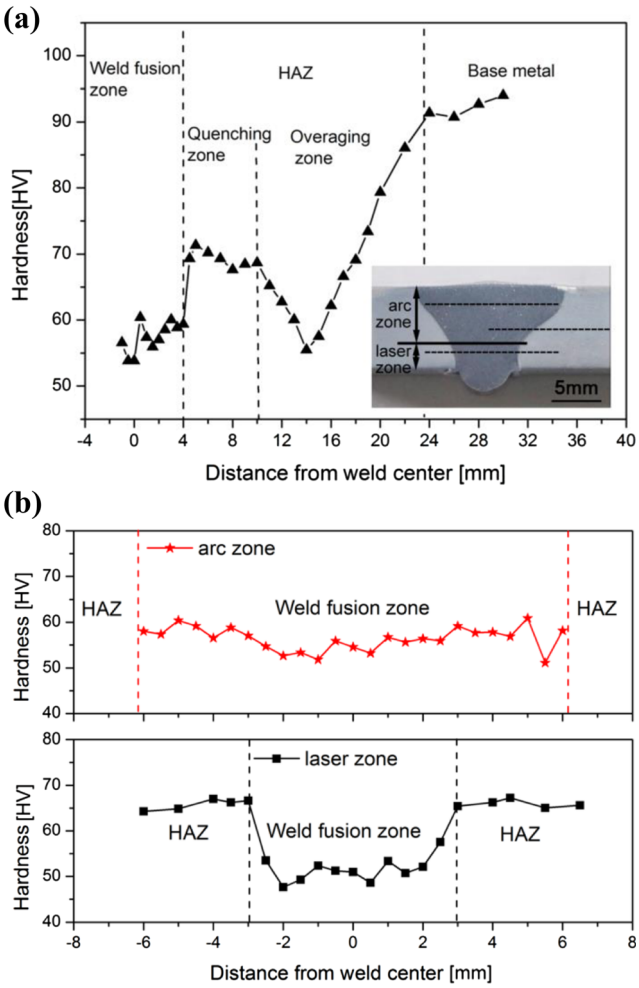

Fig. 4 Hardness distribution of the hybrid laser-MIG welded joint: **a** different zones and **b** weld fusion zone

The weld fusion zone of hybrid laser-arc welded joint consists of arc zone and laser zone [17, 18]. As shown in Fig. 5b, c, the grain size of laser zone is larger than that of arc zone. And, the precipitates of laser zone are fewer and more scattered when compared with those in arc zone.

As shown in Fig. 5d, the width of the PMZ is about 400 μm, which consists of irregular polygonal grains of 10–100 μm (Fig. 5e). Light-colored Al-rich band can be observed along the grain boundaries. The microstructure of quenched zone is shown in Fig. 5f. Many dot-like precipitated particles uniformly distribute in α-Al matrix. The microstructure does not show preferred orientations. Figure 6a shows a large number of irregular grains uniformly distributed in quenched zone [19].

It can be observed that some irregular white zones distribute randomly in the over-aging zone (Fig. 5g). With increasing distance from weld center, the shape of white zone changes from irregular to slender (Fig. 5g–i). As shown in Fig. 5h, fiber-like grains can be found in HAZ 20 mm away from the weld center. It is similar to the microstructure of base metal (Fig. 5i). The grain distribution of over-aging zone is also similar to that of base metal (Fig. 6b–d). The grains are elongated along the direction of extrusion, with size of 5–30 μm in width and 10–150 μm in length. Many evenly distributed dot-like precipitated particles and some coarse black particles can be observed in Fig. 5e–i.

The coarse particles in base metal were analyzed by SEM equipped with EDS. The particles of 1–10 μm in Fig. 7a are rich in Fe, Mn, and Si. Dot-like precipitated particles cannot be measured in SEM image of the base metal. SEM images of the quenched zone and the over-aging zone are similar to that of the base metal. Figure 7b shows the SEM image of the weld fusion zone. The particles (0.5–3 μm) observed in the weld fusion zone are rich in Mg, Fe, and Si. The filler metal used is Al-Mg welding wire. The phases that may be observed in the weld fusion zone are β (Al_8Mg_5/Al_3Mg_2), Mg_2Si, Al_3Fe, and $Al_6(FeMn)$. A detailed study by TEM will be shown in the next section.

3.3 TEM analysis and thermal cycles

Figure 8 shows the TEM images of base metal, HAZ, and weld metal of hybrid laser-MIG welded joint. Three types of precipitates can be observed in the base metal: y small needle-like precipitates of several hundred nanometers in length, (2) block-shaped precipitates 30–

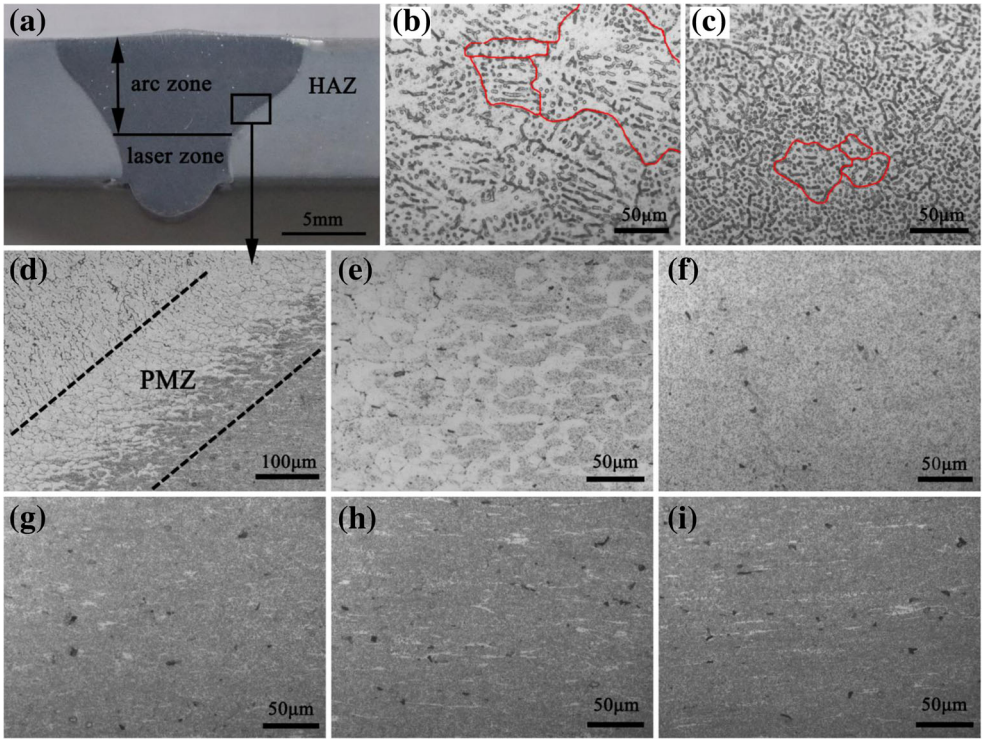

Fig. 5 Macrostructure and microstructure of the hybrid laser-MIG welded A6N01S-T5 joint: **a** the cross-sectional image, **b** laser zone, **c** arc zone, **d** high magnification of the selected region in **a**, **e** partially melted zone (PMZ), **f** quenched zone, **g**, **h** over-aging zones which is 15 and 20 mm away from weld center, and **i** base metal

240 nm in size, and (3) rod-like precipitates of 10–20 nm in width and 500 nm in length.

The precipitation sequence of Al-Mg-Si alloy has generally been reported as follows [1]: supersaturated solid solution → clusters with varying Mg and Si content → GP zones → β'' → $\beta' + B' + U1 + U2$ → β-Mg_2Si. As reported in previous study, β' phase is a rod-shape precipitate with several hundred nanometers long and about 15-

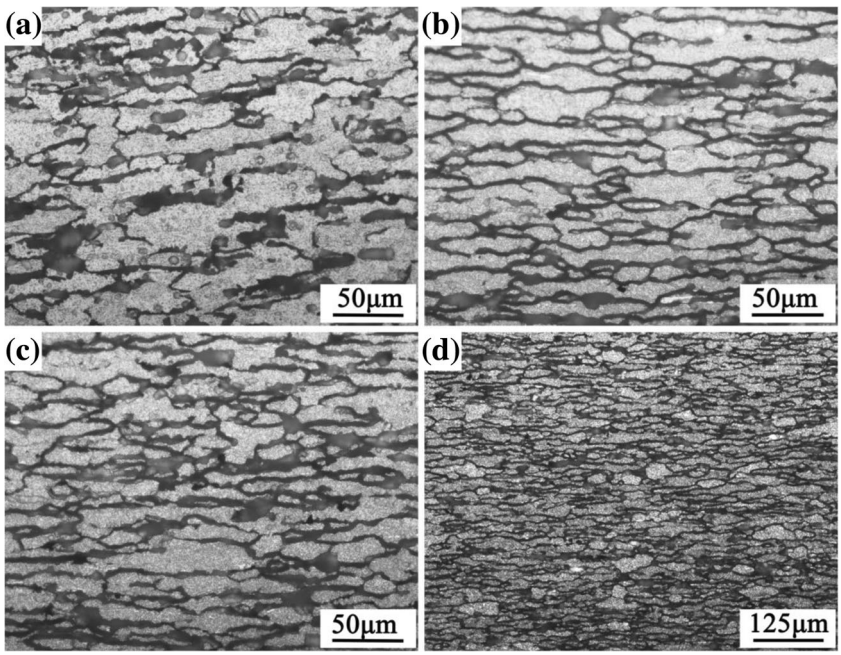

Fig. 6 Grain distributions of the hybrid laser-MIG welded joint: **a** quenched zone, **b** over-aging zone which is 15 mm from weld center, and **c**, **d** base metal

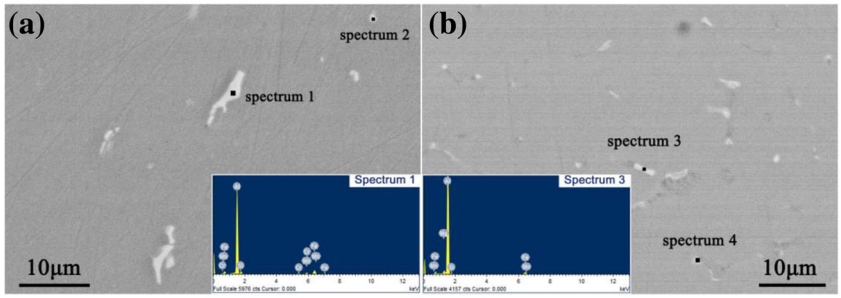

Fig. 7 SEM images and EDS analysis of the hybrid laser-MIG welded joint: **a** base metal and **b** weld fusion zone

Element	Spectrum 1		Spectrum 2		Spectrum 3		Spectrum 4	
	Weight%	Atomic%	Weight%	Atomic%	Weight%	Atomic%	Weight%	Atomic%
Mg K	-	-	-	-	2.05	2.39	5.61	6.46
Al K	72.63	82.00	86.96	91.30	86.11	90.56	84.99	88.18
Si K	5.51	5.97	4.14	4.18	2.04	2.06	1.32	1.31
Cr K	1.72	1.01	-	-	-	-	-	-
Mn K	3.98	2.21	1.41	0.73	1.00	0.51	-	-
Fe K	16.17	8.82	7.49	3.80	8.80	4.47	8.09	4.05
Totals	100.00		100.00		100.00		100.00	

nm diameter [1, 20]. So, the needle-like precipitates in Fig. 8a are β' phases, which are the major strengthening phases of A6N01S-T5 alloy.

Dispersoids containing Mn and/or Cr can be observed in Al-Mg-Si alloy with small amount of Mn and Cr [21, 22]. Rod- and spherical-shaped Mn dispersoids of sizes in the range of 100–200 nm distributed uniformly in the matrix of the examined Al-Mg-Si-Cu alloy with high Mn content were proved by Han et al. [21]. Liu et al. [20] pointed out that there were a considerable amount of coarse dispersoids randomly distributed in 6061-T6 Al alloy. This implies that the rod-like precipitates and block-shaped precipitates in Fig. 8a are dispersoids, which does not have precipitation hardening effect on the base metal.

According to the selected area electron diffraction (SAED) pattern analysis, Al_8Mn_5 precipitates are existed. Corresponding to coarse dark precipitates in Figs. 5e–i and 6a, large precipitates can also be observed in the TEM images (Fig. 8b). EDS results in Fig. 6a and SAED pattern analysis in Fig. 8b indicate that these precipitates are $Al_9Fe_{0.84}Mn_{2.16}Si$ phase.

The thermal cycles (Fig. 9) produced the peak temperatures of 639, 367, 326, and 223 °C at the positions of 5, 10, 15, and 20 mm, respectively. Milkereit et al. [23] indicated that all Al-Mg-Si alloys (6060, 6063, 6005A, and 6082) show similar precipitation behavior, consisting of high-temperature (500–400 °C) precipitation of at least the Mg_2Si phase and the low-temperature (350–300 °C) precipitation of presumably β'/B'. β' phases are almost not affected at the location of 20 mm away from the weld center because the peak temperature is lower than the solid solution temperature of β'.

At the locations of 5, 10, and 15 mm away from the weld center, the peak temperature is higher than the solid solution temperature of β', and dissolution of β' phases occurs. As shown in Fig. 8d, small needle-like β' phase cannot be observed at the location about 15 mm away from weld center, which is the most softened part in over-aging zone. But, there are many small-size (~40 nm) precipitates distributed in the grains. This indicates that β' phases are dissolved and a lot of dot-like particles precipitate due to the thermal effect during welding process. But, dispersoids still exist in the grains and at the grain boundaries. Al_8Mn_5 precipitates can also be found (Fig. 8d).

As shown in Fig. 8e, f, Mg_2Si phases and large irregular precipitations can be observed in weld fusion zone. The size of Mg_2Si phases is about 500 nm in width and 1000 nm in length, which is much larger than β' phase in the base metal and dot-like precipitations in over-aging zone. Figure 8f is an enlarged view of the precipitations distributed in the dendrites shown in Fig. 7b. It is certain that there are no other particles around the large irregular precipitations.

3.4 Relationship between microstructures and hardness distribution

Precipitation strengthening is the major strengthening mechanism of Al-Mg-Si alloy series. In addition, the strengthening mechanism also includes solid solution strengthening, interface strengthening, and dislocation strengthening [24].

The grain size of over-aging zone and base metal has little difference, as discussed in Sect. 3.2. Therefore, the grain distribution has little effect on the hardness. Based on the analysis of TEM images, β' phase dissolved due to the thermal influence of the welding process. As the β' phases are the major strengthening phases in A6N01S-T5, precipitation strengthening in the over-aging zone is decreased. In accordance with this result, the reduction of hardness in over-aging zone is closely related to the decrease of precipitation strengthening [25, 26].

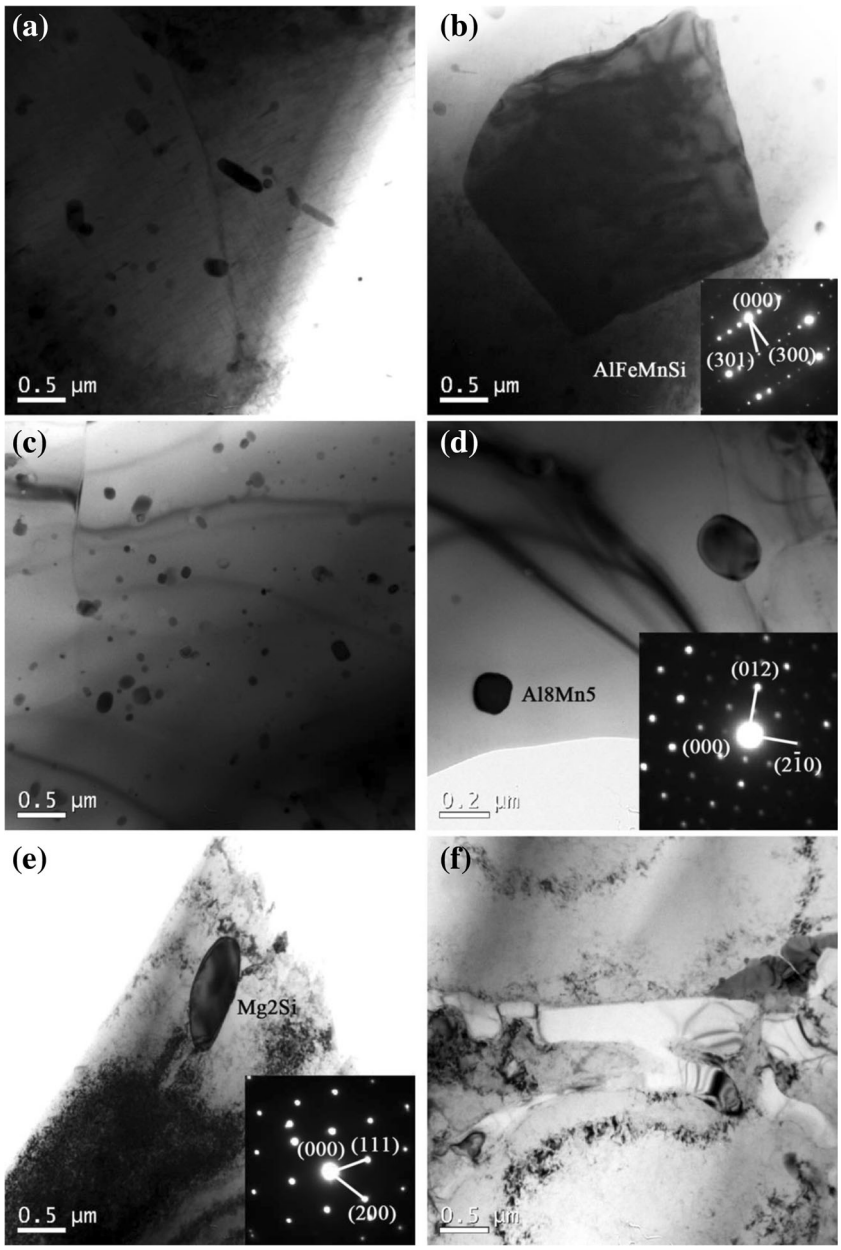

Fig. 8 TEM images of the hybrid laser-MIG welded joint: **a** base metal, **b** $Al_9Fe_{0.84}Mn_{2.16}Si$ phase in base metal, **c** the most softened part in over-aging zone, **d** Al_8Mn_5 phase in over-aging zone, **e** Mg_2Si in the fusion zone, and **f** precipitations in the fusion zone

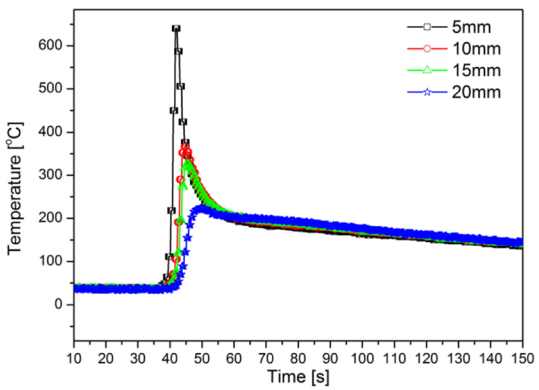

Distance from weld center [mm]	Peak temperature [°C]
5	639
10	367
15	326
20	223

Fig. 9 Thermal cycles of hybrid welding

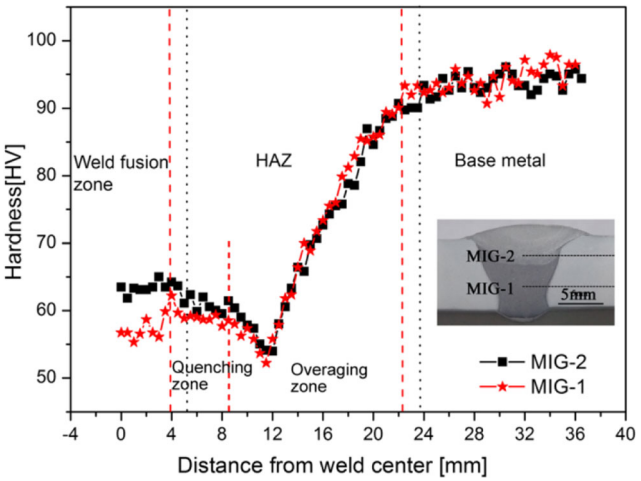

Fig. 10 Hardness distribution of the MIG welded joint

The hardness of the filler wire ER5356 is much lower than the base metal. And, the sizes of Mg_2Si phases and precipitations distributed in the fusion zone are large (Fig. 8e, f), resulting in softening in weld fusion zone. As shown in Fig. 5b, c, the grain size of laser zone is larger than that of arc zone; there are fewer precipitates in the laser zone with more scattering than that in the arc zone. According to Hall-Petch equation and precipitation strengthening mechanism, the hardness of laser zone (52 HV) is slightly lower than arc zone (56 HV).

3.5 Comparison with MIG welding method

3.5.1 The welding efficiency and heat input

As shown in Fig. 2, groove angle used in hybrid welding (60°) is smaller and thickness of root face (3 mm) is larger compared with MIG welding. In order to obtain full welding penetration and good weld formation of 8-mm-thick 6N01S-T5 plates, MIG welding needed two-layer and two-pass operation, while hybrid welding only needs single-pass welding (Table 4). The

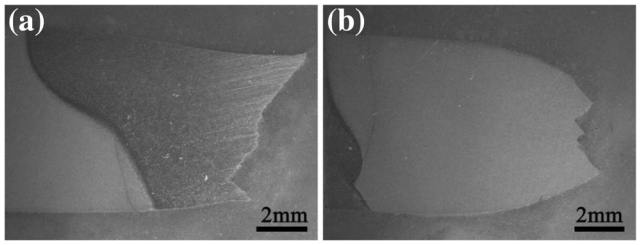

Fig. 11 Macrosections of fracture zone: **a** hybrid laser-MIG welded joint and **b** MIG welded joint

welding time needed to weld per unit length of hybrid welding is about 2.57 times as that of MIG welding.

The formula of liner energy can be simplified as $E = (P_{laser} + U_{MIG} \times I_{MIG}) / v$. Welding process parameters (P_{laser}, U_{MIG}, I_{MIG}, v) and the results of E are shown in Table 4. It can clearly be seen that the liner energy of hybrid welding process is 1.6–1.8 times as that of each pass of MIG welding process. But, the total liner energy of hybrid welding is lower than that of MIG welding.

3.5.2 Mechanical properties

As shown in Fig. 10, hardness distribution of the MIG welded joint is similar to that of the hybrid joint. The two lines are 2 and 6 mm away from the top. The hardness of layer 1 and layer 2 of the weld fusion zone is 57 and 63 HV, respectively. The softest point of MIG joint is at HAZ, which is 52 HV.

As discussed in Sect. 3.5.1, the MIG welding process consists of two layers and two passes. Layer 1 of weld fusion zone experienced twice heating and cooling process, and layer 2 of weld fusion zone only experienced one heating and cooling processes. The liner energy of the second pass welding (5.5 kJ/cm) is lower than the first pass (6.4 kJ/cm). The higher the liner energy is, the longer the existence time of molten pool is. The longer time molten pool makes larger precipitates and the larger distance between the precipitates. And, the grain size also increases with longer molten pool time. Large

Table 5 Tensile properties of A6N01S-T5 welded joints

Welding method	Tensile strength (MPa)	Fracture position	Joint efficiency (%)
Laser-MIG	242	Weld zone	83
Laser-MIG	246	Weld zone	84
Laser-MIG	242	Weld zone	83
Average	243	–	83
MIG	211	HAZ	72
MIG	209	HAZ	72
MIG	209	HAZ	72
Average	210	–	72

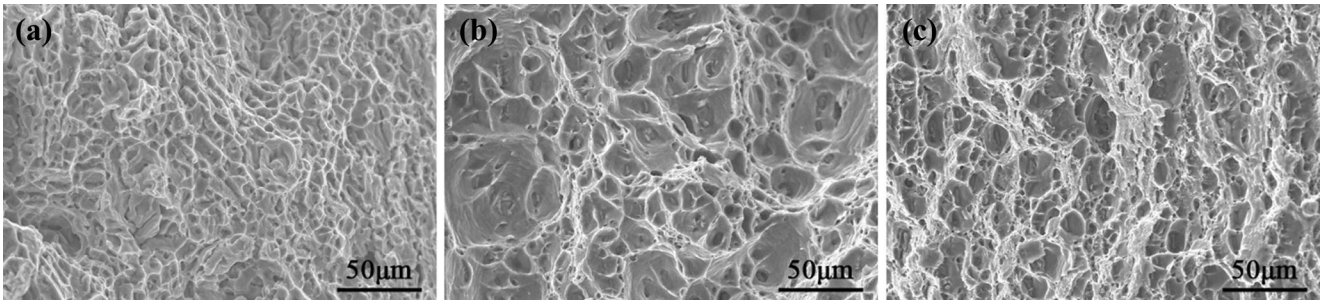

Fig. 12 SEM images of the fractured surface: **a** hybrid laser-MIG welded joint, **b** MIG welded joint, and **c** base metal

precipitates and grain size can lead to the deterioration of hardness. So, the hardness of layer 1 (57 HV) is lower than that of layer 2 (63 HV).

Although the total liner energy of MIG welding process (11.9 kJ/cm) is higher than hybrid welding process (10.3 kJ/cm), the liner energy of hybrid welding process is 1.6–1.8 times as that of each pass welding of MIG welding. So, the deterioration of the microstructure of weld fusion zone of hybrid welded joint is more serious. Furthermore, Mg would be seriously burnt out in welding molten pool because of its low melting point (650 °C) [12, 14]. Mg is a solution-strengthening element. Higher liner energy and the addition of laser melting in hybrid welding process would lead to more severe loss of Mg, reducing the contribution of Mg to the strength. Therefore, we see that the hardness of weld fusion zone of hybrid welded joint is lower than that of MIG welded joint.

For comparison, the lowest hardnesses at over-aging zone of hybrid welded joint and MIG welded joint are 56 and 52 HV, respectively. The lowest hardnesses at weld fusion zone of hybrid welded and MIG welded joints are 52 and 57 HV. The softest point of hybrid welded joint is at the weld fusion zone, while that of MIG welded joint is at HAZ.

Tensile properties for MIG and hybrid laser-MIG welded joints are given in Table 5. It is clear that the tensile strength of laser-MIG welded joint is 33 MPa higher than MIG welded joint. Joint efficiency of laser-MIG welded joint is 83 %, while MIG welded joint is only 72 %. The loss of strength can be attributed to the thermal cycles in welding process and the filler wire used. In the hybrid welded joint, fracture occurred in the weld zone, while in MIG welded joint, fracture occurred in HAZ. The fracture positions of tensile tests are relevant to the softest points of the joints.

tpAs shown in Fig. 11a, the fracture surface of hybrid welded joint is at about 45° angle to the tensile direction and the fracture position has no obvious necking. The fracture surface of the base metal had similar features. But, the fracture position of MIG welded joint has apparent necking (Fig. 11b). All fractographs of hybrid laser-arc welded joints, MIG welded joints, and base metal reveal dimple patterns (Fig. 12). The fractographs of the hybrid laser-MIG welded joint show much shallower dimples than MIG welded joint and base metal, indicating its lower ductility. As shown in Fig. 12b, c, large dimples are surrounded by small dimples in the fractograph of MIG welded joint and base metal. There are many second phase particles in the dimples. And, the dimple in fractograph of MIG welded joint is obviously larger than that of the base metal.

4 Conclusion

A6N01S-T5 Al alloy was welded by hybrid laser-MIG welding method. The microstructure and mechanical properties of the joints were studied, and the following conclusions can be drawn:

1. The softest point of laser-MIG welded joint is at the weld fusion zone. Softening in the HAZ due to the welding heat input is also evident.
2. β' phases are the major strengthening phases of A6N01S-T5 alloy. The softening in HAZ of the hybrid laser-MIG welded joint is mainly due to the dissolution of β' phases. The softening in the fusion zone is owing to the addition of ER5356 filler metal and coarse precipitations.
3. Compared with MIG welding process, the welding efficiency of hybrid welding is higher. For the tensile strength, the hybrid welded joint showed an obvious advantage over the MIG welded joint. The fracture positions of the hybrid welded joint and the MIG welded joint are at the weld fusion zone and HAZ, respectively, which are relevant to the softest points of joints.

Acknowledgments This work was financially supported by the National Program on Key Basic Research Project of China (973 Program, Grant No. 2014CB660807) and the National Natural Science Foundation of China (Grant No. 51474178).

References

1. Vissers R, van Huis MA, Jansen J, Zandbergen HW, Marioara CD, Andersen SJ (2007) The crystal structure of the β′ phase in Al-Mg-Si alloys. Acta Mater 55:3815–3823
2. Yang SL, Lin QL (2012) Microstructures and mechanical properties of A6N01 aluminum alloy welding joint. Chin J Nonferrous Metals 22:2720–2725
3. Gou GQ, Huang N, Chen H, Liu HM, Tian AQ, Guo ZC (2012) Research on corrosion behavior of A6N01S-T5 aluminum alloy welded joint for high-speed trains. J Mech Sci Technol 26:1471–1476
4. Ribic B, Palme TA, DebRoy T (2009) Problems and issues in laser-arc hybrid welding. Int Mater Rev 54:223–244
5. Zhang C, Li G, Gao M, Yan J, Zeng XY (2013) Microstructure and process characterization of laser-cold metal transfer hybrid welding of AA6061 aluminum alloy. Int J Adv Manuf Technol 68:1253–1260
6. Campana G, Ascari A, Fortunato A, Tani G (2009) Hybrid laser-MIG welding of aluminum alloys: the influence of shielding gases. Appl Surf Sci 255:5588–5590
7. Moradi M, Ghoreishi M, Frostevarg J, Kaplan AFH (2013) An investigation on stability of laser hybrid arc welding. Opt Lasers Eng 51:481–487
8. Ascari A, Fortunato A, Orazi L, Campana G (2012) The influence of process parameters on porosity formation in hybrid LASER-GMA welding of AA6082 aluminum alloy. Opt Laser Technol 44:1485–1490
9. Ola OT, Doern FE (2015) Keyhole-induced porosity in laser-arc hybrid welded aluminium. Int J Adv Manuf Technol 80:3–10
10. Gao M, Chen C, Mei SW, Wang L, Zeng XY (2014) Parameter optimization and mechanism of laser-arc hybrid welding of dissimilar Al alloy and stainless steel. Int J Adv Manuf Technol 74:199–208
11. Hu B, Richardson IM (2007) Microstructure and mechanical properties of AA7075(T6) hybrid laser/GMA welds. Mater Sci Eng A 459:94–100
12. Yan SH, Nie Y, Zhu ZT, Chen H, Gou GQ, Yu JP, Wang GG (2014) Characteristics of microstructure and fatigue resistance of hybrid fiber laser-MIG welded Al-Mg alloy joints. Appl Surf Sci 298:12–18
13. Yan J, Gao M, Li G, Zhang C, Zeng XY, Jiang M (2013) Microstructure and mechanical properties of laser-MIG hybrid welding of 1420 Al-Li alloy. Int J Adv Manuf Technol 66:1467–1473
14. Yan SH, Chen H, Zhu ZT, Gou GQ (2014) Hybrid laser-metal inert gas welding of Al-Mg-Si alloy joints: microstructure and mechanical properties. Mater Des 61:160–167
15. Yan J, Zeng XY, Gao M, Lai J, Lin TX (2009) Effect of welding wires on microstructure and mechanical properties of 2A12 aluminum alloy in CO2 laser-MIG hybrid welding. Appl Surf Sci 255:7307–7313
16. Mutombo K, du Toit M (2011) Corrosion fatigue behaviour of aluminium alloy 6061-T651 welded using fully automatic gas metal arc welding and ER5183 filler alloy. Int J Fatigue 33:1539–1547
17. Casalino G, Mortello M, Leo P, Benyounis KY, Olabi AG (2014) Study on arc and laser powers in the hybrid welding of AA5754 Al-alloy. Mater Des 61:191–198
18. Gao M, Zeng XY, Yan J, Hu QW (2008) Microstructure characteristics of laser-MIG hybrid welded mild steel. Appl Surf Sci 254:5715–5721
19. Wang YJ, Liao HC, Wu YN, Yang J (2014) Effect of Si content on microstructure and mechanical properties of Al-Si-Mg alloys. Mater Des 53:634–638
20. Liu HJ, Hou JC, Guo H (2013) Effect of welding speed on microstructure and mechanical properties of self-reacting friction stir welded 6061-T6 aluminum alloy. Mater Des 50:872–878
21. Han Y, Ma K, Li L, Chen W, Nagaumi H (2012) Study on microstructure and mechanical properties of Al-Mg-Si-Cu ally with high manganese content. Mater Des 39:418–424
22. Lodgaard L, Ryum N (2000) Precipitation of dispersoids containing Mn and/or Cr in Al-Mg-Si alloys. Mater Sci Eng A 283:144–152
23. Milkereit B, Wanderka N, Schick C, Kessler O (2012) Continuous cooling precipitation diagrams of Al-Mg-Si alloys. Mater Sci Eng A 550:87–96
24. Huang XY (2008) The microstructure of materials and its electron microscopy analysis. Metallurgical Industry, Beijing
25. Aval HJ, Serajzadeh S (2014) A study on natural aging behavior and mechanical properties of friction stir-welded AA6061-T6 plates. Int J Adv Manuf Technol 71:933–941
26. Dehghani K, Ghorbani R, Soltanipoor AR (2015) Microstructural evolution and mechanical properties during the friction stir welding of 7075-O aluminum alloy. Int J Adv Manuf Technol 77:1671–1679